



**HAL**  
open science

# Superconductivity in monolayer and few-layer graphene: II. Topological edge states and Chern numbers

Adeline Crépieux, Emile Pangburn, Louis Haurie, Oladunjoye Awoga, Annica Black-Schaffer, Nicholas Sedlmayr, Catherine Pépin, Cristina Bena

## ► To cite this version:

Adeline Crépieux, Emile Pangburn, Louis Haurie, Oladunjoye Awoga, Annica Black-Schaffer, et al.. Superconductivity in monolayer and few-layer graphene: II. Topological edge states and Chern numbers. Physical Review B, 2023, 108 (13), pp.134515. 10.1103/PhysRevB.108.134515 . cea-04259581

**HAL Id: cea-04259581**

**<https://cea.hal.science/cea-04259581>**




Submitted on 26 Oct 2023

**HAL** is a multi-disciplinary open access archive for the deposit and dissemination of scientific research documents, whether they are published or not. The documents may come from teaching and research institutions in France or abroad, or from public or private research centers.

L'archive ouverte pluridisciplinaire **HAL**, est destinée au dépôt et à la diffusion de documents scientifiques de niveau recherche, publiés ou non, émanant des établissements d'enseignement et de recherche français ou étrangers, des laboratoires publics ou privés.

# Superconductivity in monolayer and few-layer graphene.

## II. Topological edge states and Chern numbers

Adeline Crépieux <sup>1</sup>, Emile Pangburn,<sup>2</sup> Louis Haurie,<sup>2</sup> Oladunjoye A. Awoga <sup>3</sup>, Annica M. Black-Schaffer,<sup>4</sup> Nicholas Sedlmayr <sup>5</sup>, Catherine Pépin,<sup>2</sup> and Cristina Bena<sup>2</sup>


<sup>1</sup>Aix Marseille Univ, Université de Toulon, CNRS, CPT, Marseille, France

<sup>2</sup>Institut de Physique Théorique, Université Paris Saclay, CEA CNRS, 91190 Gif-sur-Yvette Cedex, France

<sup>3</sup>Solid State Physics and NanoLund, Lund University, Box 118, S-221 00 Lund, Sweden

<sup>4</sup>Department of Physics and Astronomy, Uppsala University, Box 516, S-751 20 Uppsala, Sweden

<sup>5</sup>Institute of Physics, Maria Curie-Skłodowska University, PL-20031 Lublin, Poland

 (Received 24 January 2023; revised 27 March 2023; accepted 31 March 2023; published 25 October 2023)

We study the emergence of electronic edge states in superconducting monolayer, bilayer, and trilayer graphene for both spin-singlet and spin-triplet superconducting order parameters. We focus mostly on the gapped chiral  $p + ip'$ - and  $d + id'$ -wave superconducting states that show a nonzero Chern number and a corresponding number of edge states. For the  $p + ip'$ -wave state, we observe a rich phase diagram for the Chern number when tuning the chemical potential and the superconducting order parameter amplitude, which depends strongly on the number of layers and their stacking and is also modified by trigonal warping. At small parameter values, compared to hopping energy, we observe a region whose Chern number is unique to rhombohedrally stacked graphene and is independent of the number of layers. Our results can be understood in relation not only to the superconducting order parameter winding as expected but also to the normal state band structure. This observation establishes the importance of the normal state characteristics for understanding the topology in superconducting graphene systems.

DOI: [10.1103/PhysRevB.108.134515](https://doi.org/10.1103/PhysRevB.108.134515)

### I. INTRODUCTION

Superconductivity in graphene systems have generated a lot of interest lately, mainly due to its experimental discovery in twisted bilayer graphene [1] and more recently in trilayer rhombohedral (or ABC) graphene [2]. The fact that the superconductivity discovered in twisted bilayer graphene has similarities to the physics of cuprates makes one wonder if the study of graphene may also shed light on the physics of exotic high-temperature superconductors and eventually help with creating superconductors with higher critical temperatures. This has led to an immense ongoing effort to unravel the nature of the superconducting (SC) state of twisted bilayer graphene [3–25]. On the other hand, for rhombohedral graphene, its nontrivial normal state suggests that the superconducting phase is likely exotic, which has led to several theoretical proposals for the SC mechanism [26–34]. However, even if the attention of the community has been directed toward multilayer graphene, the interest in understanding superconductivity in monolayer graphene has also not waned. In fact, an enormous effort has been put into studying the possibility of intrinsic superconductivity in monolayer graphene, as well as into understanding its characteristics [35–46]. More recently, one has also focused on inducing an exotic SC state in graphene via a proximity effect [47–52]. These developments have also generated a widespread interest in other graphene systems with different stacking [53–61].

One of the main pressing questions to be answered is the nature of the superconducting state in different graphene systems. Many different methods, including mean-field theory

[35,40,41,62], renormalization group [36–39,63], Monte Carlo [43,64–66], and others, have predicted both spin-singlet and spin-triplet order parameters, beyond conventional  $s$  pairing, such as  $d$ -,  $p$ - and  $f$ -wave states [12,16,25,35,36,66–73]. Understanding the type of order parameter developed by these systems may help in making progress in understanding the underlying mechanism giving rise to superconductivity, be it phonon based [6,28,71] and enhanced by the formation of flat bands in the multilayer graphene spectrum, such as in twisted bilayer [74] or rhombohedral graphene [28], or electron-electron interaction induced and also enhanced by the flat band formation [8,33,75]. Depending on the nature of the order parameter, the question also arises about the possibility of generating topological edge and corner states and eventually putative Majorana states [76,77].

In a recent work [78] we have examined the most energetically favorable symmetry-allowed superconducting states in monolayer graphene, as well as in bilayer and ABA and ABC trilayer graphene in order to lay the basis for the understanding of their fundamental characteristics. Thus we have calculated the band structure which would be visible using angle-resolved photoemission spectroscopy and the density of states, measurable in scanning tunneling spectroscopy, and in this way distinguished between nodal ( $d_{xy}$ -,  $d_{x^2-y^2}$ -,  $p_x$ -,  $p_y$ -wave) and gapped ( $s_{\text{on}}$ -,  $s_{\text{ext}}$ -,  $p + ip'$ -,  $d + id'$ -,  $f$ -wave) order parameters, arising from onsite, nearest-neighbor (NN), or next-to-nearest neighbor (NNN) pairing ranges. We have also examined the gap-closing points arising in the spectrum when varying the chemical potential and the superconducting

order parameter. For the multilayer systems we additionally have examined the effects of the trigonal warping.

In the present work we continue this analysis by studying the nontrivial topology of several of the SC states. We do so by both calculating the Chern number and studying their topologically protected edge states. The main systems we are here focusing on are those exhibiting  $d + id'$ - and  $p + ip'$ -wave symmetry order parameters, which are both topological as they are both chiral states [40,79,80] and display a hard energy gap in the spectrum, for which the formation of topological edge states is easy to distinguish [42,76,81]. We find that for the  $d + id'$ -wave SC state, the Chern number is roughly independent of the system parameters such as the chemical potential and the SC order parameter, while for the  $p + ip'$ -wave state we obtain rich phase diagrams which depend on the number of layers, as well as on the type of stacking for the multilayer systems. We also find that the trigonal warping has a significant effect on the topological phase diagram at large values of the chemical potential and the SC order parameter. One of our most intriguing observations is that for both  $d + id'$  and  $p + ip'$  multilayer samples at small chemical potential and SC order parameter there is a small region whose size depends on the value of the interlayer hopping, and whose Chern number for rhombohedral, ABC-stacked, graphene does in fact not depend on the number of layers. This observation can be used to identify rhombohedral ABC-stacked graphene from other types of stacking.

Our results indicate that the value of the Chern number is not only tied to the winding of the SC order parameter as expected [40,79,80] but is also strongly correlated to the normal-state band structure. In fact, for a  $p + ip'$  order parameter, we note that for chemical potentials below the van Hove singularity, each spin state filled band contributes a Chern number of 2, since the SC order parameter winds once around each of the two Fermi surfaces localized around the Dirac  $K$  and  $K'$  points in the Brillouin zone. On the other hand, for a chemical potential above the van Hove singularity, each spin-state band contributes a Chern number of 1, given that in this regime the system has only one Fermi surface centered around the  $\Gamma$  point. For multilayer systems we can likewise predict the Chern number by counting the bands and examining the normal-state Fermi surface topology.

We complement our Chern number calculations by a calculations of the edge states in both chiral SC states. We use a technique developed recently [82], which relies on the fact that the spectral function in a semi-infinite system can be obtained by introducing a scalar linelike impurity in an infinite system and using the  $T$ -matrix formalism. Our obtained edge energy spectra confirm that the number of observed edge states corresponds to the bulk Chern number following the bulk-boundary correspondence [83,84]. The only exception are a few irregular cases for which extra unprotected zero-energy crossings are observed in the spectrum. Besides the gapped  $d + id'$ - and  $p + ip'$ -wave states, we find that the gapless  $d_{xy}$ -wave system also shows interesting edge properties, related to its nodal superconductivity, which we briefly review.

The rest of the article is organized as follows. In Sec. II we present the formalism used to describe the SC states in graphene and how to calculate the Chern number and the correction to the spectral function in the presence of an

edge. The results obtained for monolayer, bilayer, and trilayer graphene are discussed in Secs. III, IV, and V, respectively. We summarize our results in Sec. VI.

## II. MODEL AND METHOD

We start by introducing the model and Hamiltonian for superconductivity in graphene systems. We then introduce the formula for how to calculate the Chern number, followed by the technique of extracting the edge spectral function.

### A. Superconducting Hamiltonian

We are primarily interested in describing the chiral SC states in graphene systems, which can be modeled as pairing on intralayer NN bonds [35,78]. For single-layer graphene with SC pairing induced on NN bonds, the Hamiltonian  $H_{\mathbf{k}}$  is given by a Fourier transform of the real-space Hamiltonian  $H = H_0 + H_{\text{NN}}$ , where

$$H_0 = -t \sum_{(i,j),\sigma} [a_{i\sigma}^\dagger b_{j\sigma} + b_{j\sigma}^\dagger a_{i\sigma}] - \mu \sum_{i\sigma} [a_{i\sigma}^\dagger a_{i\sigma} + b_{i\sigma}^\dagger b_{i\sigma}] \quad (1)$$

is the noninteracting Hamiltonian, with  $t$  the NN hopping parameter between neighboring A and B sites indexed by  $i$  and  $j$ ,  $\mu$  the chemical potential, while  $a_{i\sigma}^\dagger$  ( $a_{i\sigma}$ ) and  $b_{i\sigma}^\dagger$  ( $b_{i\sigma}$ ) are the creation (annihilation) operators for the A and B lattice sites of the graphene honeycomb lattice. The SC Hamiltonian for the spin-singlet channel ( $\eta = 0$ ) and for the spin-triplet channels ( $\eta = x, y, z$ ) is given by [75,78]

$$H_{\text{NN}}^0 = \sum_{(ij)} \Delta_{ij}^0 (a_{i\uparrow}^\dagger b_{j\downarrow}^\dagger - a_{i\downarrow}^\dagger b_{j\uparrow}^\dagger) + \text{H.c.}, \quad (2)$$

$$H_{\text{NN}}^x = \sum_{(i,j)} \Delta_{ij}^x (a_{i\uparrow}^\dagger b_{j\uparrow}^\dagger - a_{i\downarrow}^\dagger b_{j\downarrow}^\dagger) + \text{H.c.}, \quad (3)$$

$$H_{\text{NN}}^y = i \sum_{(i,j)} \Delta_{ij}^y (a_{i\uparrow}^\dagger b_{j\uparrow}^\dagger + a_{i\downarrow}^\dagger b_{j\downarrow}^\dagger) + \text{H.c.}, \quad (4)$$

$$H_{\text{NN}}^z = \sum_{(i,j)} \Delta_{ij}^z (a_{i\uparrow}^\dagger b_{j\downarrow}^\dagger + a_{i\downarrow}^\dagger b_{j\uparrow}^\dagger) + \text{H.c.}, \quad (5)$$

where  $\Delta_{ij}^\eta$  is the NN SC order parameter in channel  $\eta$ . Fourier transforming into reciprocal space we arrive at

$$H_{\text{NN}}^0 = \sum_{\mathbf{k}} h_{\text{NN}}^0(\mathbf{k}) (a_{\mathbf{k}\uparrow}^\dagger b_{-\mathbf{k}\downarrow}^\dagger - a_{\mathbf{k}\downarrow}^\dagger b_{-\mathbf{k}\uparrow}^\dagger) + \text{H.c.}, \quad (6)$$

$$H_{\text{NN}}^x = \sum_{\mathbf{k}} h_{\text{NN}}^x(\mathbf{k}) (a_{\mathbf{k}\uparrow}^\dagger b_{-\mathbf{k}\uparrow}^\dagger - a_{\mathbf{k}\downarrow}^\dagger b_{-\mathbf{k}\downarrow}^\dagger) + \text{H.c.}, \quad (7)$$

$$H_{\text{NN}}^y = i \sum_{\mathbf{k}} h_{\text{NN}}^y(\mathbf{k}) (a_{\mathbf{k}\uparrow}^\dagger b_{-\mathbf{k},\uparrow}^\dagger + a_{\mathbf{k},\downarrow}^\dagger b_{-\mathbf{k}\downarrow}^\dagger) + \text{H.c.}, \quad (8)$$

$$H_{\text{NN}}^z = \sum_{\mathbf{k}} h_{\text{NN}}^z(\mathbf{k}) (a_{\mathbf{k}\uparrow}^\dagger b_{-\mathbf{k}\downarrow}^\dagger + a_{\mathbf{k}\downarrow}^\dagger b_{-\mathbf{k}\uparrow}^\dagger) + \text{H.c.}, \quad (9)$$

where the form factors  $h_{\text{NN}}^\eta(\mathbf{k})$  are given in Table I for the lowest harmonic of all symmetry-allowed states. Setting  $t = 1$  as the energy scale, and the distance between two neighboring carbon atoms,  $a = 1$ , as the length scale, the only remaining tunable parameters are the chemical potential  $\mu$  and the SC order parameter amplitude  $\Delta_0$ .

TABLE I. Expressions for the form factors for the different spin-singlet and -triplet symmetries possible on NN bonds (lowest harmonics). The overall amplitude is set to  $\Delta_0$  and the distance between two NN carbon atoms is set to 1.

$\eta$	Symmetry	Form factor $h_{\text{NN}}^\eta(\mathbf{k})$
0	$s_{\text{ext}}$	$h_{\text{NN}}^{0,s_{\text{ext}}}(\mathbf{k}) = -\frac{\Delta_0}{\sqrt{3}}e^{-ik_y}[1 + 2e^{\frac{3i}{2}k_y}\cos(\frac{\sqrt{3}}{2}k_x)]$
0	$d_{x^2-y^2}$	$h_{\text{NN}}^{0,d_{x^2-y^2}}(\mathbf{k}) = \frac{2\Delta_0}{\sqrt{6}}e^{-ik_y}[1 - e^{\frac{3i}{2}k_y}\cos(\frac{\sqrt{3}}{2}k_x)]$
0	$d_{xy}$	$h_{\text{NN}}^{0,d_{xy}}(\mathbf{k}) = \Delta_0\sqrt{2}ie^{\frac{i}{2}k_y}\sin(\frac{\sqrt{3}}{2}k_x)$
$x$	$p_y$	$h_{\text{NN}}^{\eta,p_y}(\mathbf{k}) = \frac{2\Delta_0}{\sqrt{6}}e^{-ik_y}[1 - e^{\frac{3i}{2}k_y}\cos(\frac{\sqrt{3}}{2}k_x)]$
$x$	$p_x$	$h_{\text{NN}}^{\eta,p_x}(\mathbf{k}) = i\sqrt{2}\Delta_0e^{\frac{i}{2}k_y}\sin(\frac{\sqrt{3}}{2}k_x)$

For a superconducting multilayer graphene the pairing is intralayer and the Hamiltonian is given by

$$H = \sum_{\ell=1}^L (H_0^\ell + H_{\text{NN}}^{\eta,\ell}) + H_{\text{interlayer}}, \quad (10)$$

where  $L$  is the number of layers,  $H_0^\ell$  and  $H_{\text{NN}}^{\eta,\ell}$  are the noninteracting Hamiltonian and the SC Hamiltonian associated with each layer  $\ell$ , respectively, and given by expressions equivalent to Eqs. (1)–(5), while  $H_{\text{interlayer}}$  is the coupling Hamiltonian between adjacent layers, see, e.g., Ref. [78]. Here we retain three important parameters in  $H_{\text{interlayer}}$ : (1) the interlayer hopping  $\gamma_1$  between atoms directly on top of each other; (2) the interlayer hopping  $\gamma_3$  between an atom  $A$  in one layer and the neighboring  $B$  atoms in the adjacent layer [85,86] also denoted as trigonal warping, often neglected, although of the same order of magnitude as  $\gamma_1$ ; and (3) a putative phase difference  $\phi$  between the SC order parameters in two adjacent layers.

For the calculations, the reciprocal space Hamiltonian  $H_{\mathbf{k}}$  in each layer  $\ell$  is written in the basis

$$\mathcal{B}_\ell = (a_{k\ell\uparrow}, b_{k\ell\uparrow}, a_{k\ell\downarrow}, b_{k\ell\downarrow}, a_{-k\ell\uparrow}^\dagger, b_{-k\ell\uparrow}^\dagger, a_{-k\ell\downarrow}^\dagger, b_{-k\ell\downarrow}^\dagger)^T, \quad (11)$$

such that

$$H_{\mathbf{k}} = \frac{1}{2}\mathcal{B}^\dagger H_{\text{BdG}}\mathcal{B}, \quad (12)$$

where  $\mathcal{B}$  is the basis combining all individual-layer bases  $\mathcal{B}_\ell$  and  $H_{\text{BdG}}$  is the  $8L \times 8L$  Bogoliubov-de-Gennes (BdG) Hamiltonian matrix. The factor 8 corresponds to a product of two spins, two sublattices, and the particle-hole doubling of the degrees of freedom in the BdG formalism. Since there are no spin-flip terms in the graphene systems of interest, all bands are spin degenerate. Thus, in what follows all edge and impurity states are always doubly degenerate.

### B. Chern number

To calculate the Chern number for the various SC states, we use the following expression [87–89]:

$$\mathcal{C} = \frac{i}{8\pi^2} \int d\mathbf{k} dE \text{Tr}[G^2(\mathbf{k}, E)(\partial_{k_y} H_{\mathbf{k}})G(\mathbf{k}, E)(\partial_{k_x} H_{\mathbf{k}} - G^2(\mathbf{k}, E)(\partial_{k_x} H_{\mathbf{k}})G(\mathbf{k}, E)(\partial_{k_y} H_{\mathbf{k}})], \quad (13)$$

where  $G(\mathbf{k}, E) = (iE - H_{\text{BdG}})^{-1}$  is the Matsubara Green's function. We note that as a consequence of the spin

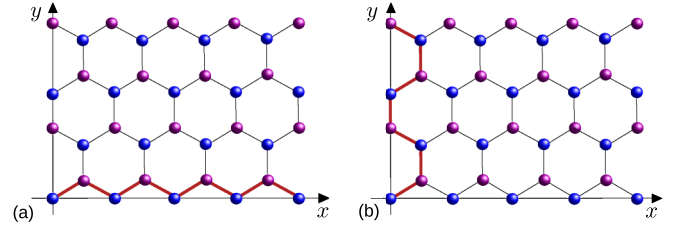


FIG. 1. Graphene lattice with A and B sites in different colors and with an impurity line (bold line) along (a) a zigzag edge and (b) an armchair edge.

degeneracy of each band, the Chern numbers in what follows are always doubled compared to studies in which this doubling has been resolved [40,76,79–81].

### C. Edge spectral function

In honeycomb graphene lattices an edge can have different orientations. We restrict our study to the two most common, armchair and zigzag edges, depicted in Fig. 1. The energy spectrum of these edges can be extracted by considering a line-like impurity parallel to the edge which cuts the system into two semi-infinite systems. Scattering of electrons due to the presence of the impurity line induces additional features in the spatially averaged electronic bulk spectral function  $A(\mathbf{k}, E)$ . The edge features are in this way captured as a correction  $\delta A(\mathbf{k}, E)$  to the bulk spectral function, given by [90,91]

$$\delta A(k_x, E) = -\frac{1}{\pi} \int_{-2\pi/3a}^{2\pi/3a} \frac{dk_y}{L_{\text{BZ},y}} \text{Im}\{\text{Tr}_{\text{el}}[G^r(\mathbf{k}, E) \times T(k_x, k_x, E)G^r(\mathbf{k}, E)]\}, \quad (14)$$

for the zigzag edge, with  $L_{\text{BZ},y} = 4\pi/3a$ , and

$$\delta A(k_y, E) = -\frac{1}{\pi} \int_{-2\pi/\sqrt{3}a}^{2\pi/\sqrt{3}a} \frac{dk_x}{L_{\text{BZ},x}} \text{Im}\{\text{Tr}_{\text{el}}[G^r(\mathbf{k}, E) \times T(k_y, k_y, E)G^r(\mathbf{k}, E)]\}, \quad (15)$$

for the armchair edge, with  $L_{\text{BZ},x} = 4\pi/\sqrt{3}a$ . Here the retarded Green's function is defined as  $G^r(\mathbf{k}, E) = (E - H_{\text{BdG}} + i0^+)^{-1}$ . The matrix trace  $\text{Tr}_{\text{el}}$  indicates that the sum is performed only over the electron degrees of freedom. The  $T$  matrix associated with a zigzag edge is defined as

$$T(k_x, k_x, E) = \left[ \mathbb{1}_n - \mathbb{V}_n \int_{-2\pi/3a}^{2\pi/3a} \frac{dk_y}{L_{\text{BZ},y}} G^r(\mathbf{k}, E) \right]^{-1} \mathbb{V}_n, \quad (16)$$

whereas for an armchair edge we have

$$T(k_y, k_y, E) = \left[ \mathbb{1}_n - \mathbb{V}_n \int_{-2\pi/\sqrt{3}a}^{2\pi/\sqrt{3}a} \frac{dk_x}{L_{\text{BZ},x}} G^r(\mathbf{k}, E) \right]^{-1} \mathbb{V}_n. \quad (17)$$

In Eqs. (16) and (17), the identity matrix  $\mathbb{1}_n$  and the impurity matrix  $\mathbb{V}_n$  are  $n \times n$  matrices with  $n = 8L$ , with the latter given

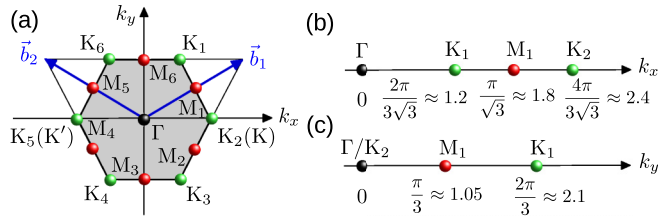


FIG. 2. (a) Schematic view of the first 2D Brillouin zone of the graphene honeycomb lattice with the 1D projections of the  $\Gamma$  (black),  $K$  (green), and  $M$  (red) points on the  $k_x$  axis in (b) and on the  $k_y$  axis in (c). The  $K_2$  and  $K_5$  points correspond to what is traditionally denoted as the  $K$  and  $K'$  points. Also depicted are the reciprocal unit vectors  $\vec{b}_{1,2} = (\pm 2\pi/\sqrt{3}, 2\pi/3)$ .

in the same basis as Eq. (12) as

$$\mathbb{V}_n = U \begin{pmatrix} 1 & 0 \\ 0 & -1 \end{pmatrix} \otimes \mathbb{1}_{n/2}, \quad (18)$$

where  $U$  is the value of the potential on the impurity line. Note that the introduced  $U$  is not a physical potential but a mathematical trick that simulates the backscattering of all electrons that reach the edge, i.e., a model of a hard boundary. Thus the value we need to use for  $U$  is *a priori* infinite, but since we cannot set it to infinity numerically, we have instead taken a very large value for  $U$  compared to the characteristic energies of the system:  $U \gg t, \mu, \Delta_0$ , and the  $\gamma$  parameters. We study the numerical convergence of our results with increasing  $U$ , and we find that convergence is reached for about  $U \approx 100t$  for the range of parameters we consider. We thus choose the value  $U = 1000t$  to ensure a very high-level precision of our numerical results. The calculations of the edge spectrum occurs in the first two-dimensional (2D) Brillouin zone which is illustrated in Fig. 2, including 1D projections for each edge direction.

### III. MONOLAYER GRAPHENE

#### A. Chern number

We start by studying monolayer graphene and first calculate the Chern number  $\mathcal{C}$  using Eq. (13). The calculation shows that  $\mathcal{C}$  is nonzero for both the  $d + id'$ - and  $p + ip'$ -wave states, whereas it is equal to zero for all the other SC states, listed in Table I, including the  $d_{xy}$ -wave state. For the  $d + id'$ -wave state, the Chern number takes a constant value equal to  $-4$  as seen in Fig. 3(a), for all values of chemical potential  $\mu$  and

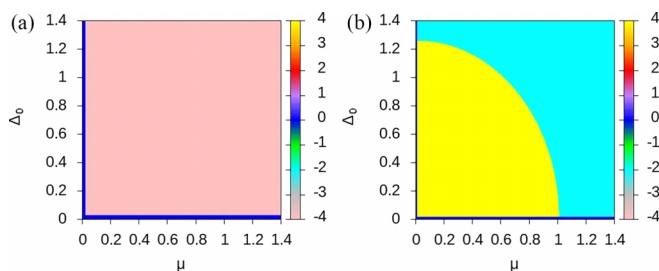


FIG. 3. Chern number  $\mathcal{C}$  as a function of  $\mu$  and  $\Delta_0$  for monolayer graphene for the (a)  $d + id'$ - and (b)  $p + ip'$ -wave states.

superconducting order parameter amplitude  $\Delta_0$ , which are the two tunable parameters. More interestingly, for the  $p + ip'$ -wave state we observe a phase transition at large values of either  $\mu$  or  $\Delta_0$ , as seen in Fig. 3(b). As shown in Ref. [78], this transition between a Chern number of 4 (yellow) and  $-2$  (cyan) corresponds to a gap closing line. The equation of this line is given by  $\Delta_0 \approx \Delta_c \sqrt{1 - (\mu/\mu_c)^2}$ , with the critical parameters  $\Delta_c \approx 1.25$  and  $\mu_c \approx 1$  (in units of  $t$ ).

The behavior of the Chern number in Fig. 3 can be understood starting from an analysis of the normal state band structure combined with the winding number of the SC order parameter [40,79]. At  $\mu < t$  and small  $\Delta_0$ , there exist two Fermi surfaces centered around the  $K$  and  $K'$  points, the Dirac points (see Appendix A). The  $p + ip'$ -wave order parameter winds once around each of these Fermi surfaces [78], thus giving a Chern number of 2 for each spin species (1 per Fermi surface), hence a total Chern number of 4. However, at  $\mu > t$  and small  $\Delta_0$ , the normal state Fermi surface undergoes a Lifshitz transition and there is then only one Fermi surface centered at the  $\Gamma$  point. The  $p + ip'$ -wave order parameter winds once per spin species around this central Fermi surface, giving a total Chern number of  $-2$  (the sign of the Chern also changes at the Lifshitz transition). This analysis holds for small  $\Delta_0$ . When  $\Delta_0$  become substantial, the border between the different Chern number regions changes, following the gap closing region established in Ref. [78].

For the  $d + id'$ -wave state, the SC order parameter winds twice around the  $\Gamma$ -centered Fermi surface due to its angular momentum, leading to a Chern number of  $-4$  for  $\mu > t$ . Here the sign of the Chern number is the same as for the  $p + ip'$ -wave state at  $\mu > t$  since they have the same winding direction. However, for  $\mu < t$ , the  $d + id'$ -wave state looks locally around the  $K$  and  $K'$  points the same as the  $p + ip'$ -wave one [40,78], except for an opposite winding at the two Dirac points. As a consequence, each Fermi surface and spin species contributes a (negative) unit to the Chern number, resulting in a  $\mathcal{C} = -4$  for the chiral  $d + id'$ -wave state also at  $\mu < t$ , and no corresponding phase transition between the large  $\mu$  and the small  $\mu$  region.

Based on this analysis it is clear that not only the winding of the SC order parameter determines the Chern number in monolayer graphene but also that the normal state band structure and its Fermi surface are crucial for understanding the results in Fig. 3.

Having established the Chern numbers for all NN pairing states in monolayer graphene, we turn to examining the edge state spectrum, as visualized by the correction to the spectral function due to a linelike impurity. We first report data for the chiral  $d + id'$ -wave and  $p + ip'$ -wave states and then finally also for the  $d_{xy}$ -wave state. We compare the number of observed edge states with the Chern number  $\mathcal{C}$ .

#### B. Edge states for $d + id'$ -wave symmetry

For the chiral  $d + id'$ -wave SC state, Fig. 3(a) shows that the Chern number  $\mathcal{C}$  takes a constant value equal to  $-4$  for any  $\mu$  and nonzero values of  $\Delta_0$ . This means that four edge states are expected at each edge, which with the spin degeneracy makes two distinguishable states [76,81]. This is verified in Fig. 4 where we plot the correction to the spectral function

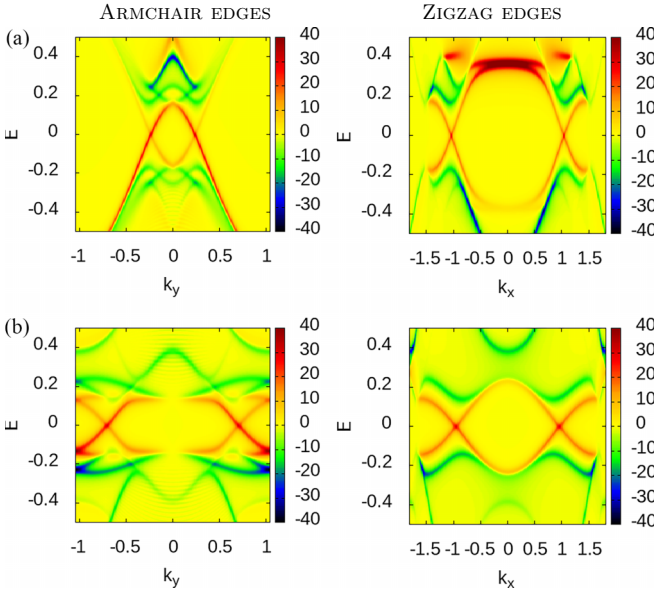


FIG. 4. Edge correction to the spectral function for monolayer graphene with a spin-singlet  $d + id'$ -wave SC order parameter with  $\Delta_0 = 0.4$  at (a)  $\mu = 0.4$  and (b)  $\mu = 1.2$ . The corresponding Chern number is  $C = -4$ .

due to a linelike impurity modeling the edge for both armchair and zigzag edges for two different values of  $\mu$  at  $\Delta_0 = 0.4$ . We observe two main characteristics: A hard energy gap of width of the order of  $\Delta_0$  opens in the spectrum and, inside this gap, a total of four states appear (red). These states are all doubly degenerate resulting in a total of eight edge states: We have checked that these states are spin degenerate by adding a Zeeman field, indeed the number of edge states doubled in the presence of magnetic field, confirming their spin degeneracy. With the Chern number  $C = -4$ , the appearance of eight edge states may at first seem to be a discrepancy, but we then note that the correction to the spectral function plotted here actually corresponds to a spatial average over the entire system, thus taking into account two edges, one on each side of the impurity line. We thus always plot the edge spectrum for two edges. In this case this gives rise to two spin-degenerate chiral and copropagating edge states on each edge, while the edge states on different edges are counterpropagating, as expected from the chirality of the SC order parameter. As a consequence, we find a full agreement between the bulk Chern number and the boundary edge states, fulfilling the bulk-boundary correspondence.

### C. Edge states for $p + ip'$ -wave symmetry

For a  $p + ip'$ -wave state the correction to the spectral function due to an impurity line along either the armchair or zigzag edge is shown in Fig. 5. Similarly to the  $d + id'$ -wave state, we observe once more the opening of a full energy gap of width of the order of  $\Delta_0$  and, inside this gap, the formation of edge states. For  $\Delta_0 = \mu = 0.4$ , we count two doubly spin-degenerate states per edge, making a total of four copropagating states per edge, see Fig. 5(a). Note that the states on opposite edges are counterpropagating. Increasing to

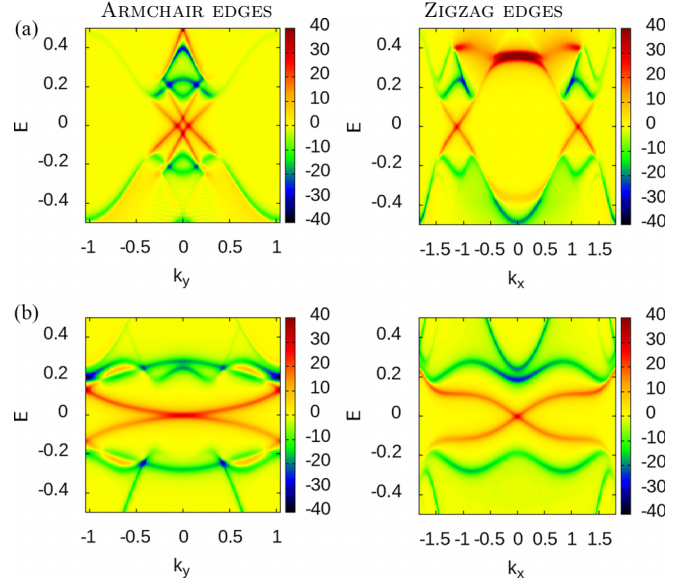


FIG. 5. Edge correction to the spectral function for monolayer graphene with a  $p + ip'$ -wave SC order parameter with  $\Delta_0 = 0.4$  at (a)  $\mu = 0.4$  corresponding to  $C = 4$ , and (b)  $\mu = 1.2$  corresponding to  $C = -2$ .

$\mu = 1.2$  we instead find two such spin-degenerate edge states, see Fig. 5(b). Both of these results are in full agreement with the values taken by  $C$ , which is equal to 4 in Fig. 5(a) and  $-2$  in Fig. 5(b).

We also note that the zero-crossing of the edge states can occur at different  $k$  values for  $\mu < t$  Fig. 5(a) and  $\mu > t$  Fig. 5(b) as well as different edge terminations. This is because the edge states will appear in the region with the lowest bulk energy gap. The bulk energy gap is set by both the normal state band structure and the SC order parameter, and is generally small around the normal-state Fermi surface. This means the minimum energy gap is found centered around the  $K$  and  $K'$  points for  $\mu < t$  and around the  $\Gamma$  point for  $\mu > t$ . Different projections of the 2D  $K$  and  $K'$ -momenta into the edge state 1D momenta for the two different edges:  $k_y = 0$ , the projection of  $K/K'$  for armchair in Fig. 2(c), and  $k_x = 2\pi/3\sqrt{3} \approx 1.2$ , the projection of  $K_1$  in Fig. 2(b) for zigzag, give rise to the different zero-energy crossing momenta for the two different edges in Fig. 2(a). However, the projection of the  $\Gamma$  point remains at zero momentum for both edges, and the edge state spectra thus appear in the vicinity of similar  $k = 0$  values in Fig. 2(b), and as a consequence the edge states for armchair and zigzag look remarkably similar when  $\mu > t$ . Thus, by increasing the value of the chemical potential, the crossing point of the edge states moves between the  $K$  and  $K'$  points to the  $\Gamma$  point.

### D. $d_{xy}$ -wave symmetry

Finally, we also report the edge spectrum for the  $d_{xy}$ -wave SC state where the Chern number  $C = 0$ , independent of the values of  $\mu$  and  $\Delta_0$ , and the system is also gapless [78]. Figure 6 displays the correction to the spectral function in the presence of an armchair edge or zigzag edge, again for  $\mu < t$  and  $\mu > t$ . Here we first note that the bulk is gapless as

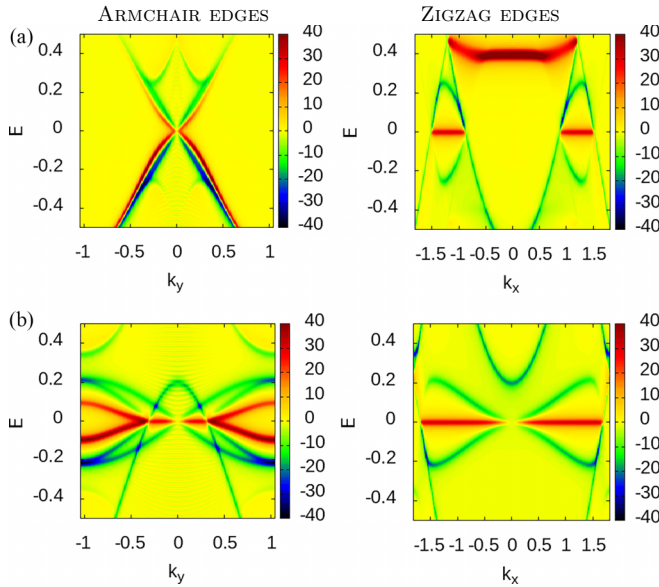


FIG. 6. Edge correction to the spectral function of monolayer graphene with a  $d_{xy}$ -wave SC order parameter with  $\Delta_0 = 0.4$  at (a)  $\mu = 0.4$  and (b)  $\mu = 1.2$ . This corresponds to a bulk  $\mathcal{C} = 0$ .

there exists green/blue lines (i.e., suppressed edge spectrum) all the way down to zero energy. Second, we see the formation of edge states (red), which in several cases consist of zero-energy flat bands. These are not of the same chiral topological origin as the edge states in the chiral  $d + id'$ - and  $p + ip'$ -wave superconductors in Figs. 4 and 5 but instead edge states found on certain surfaces in nodal superconductors. The most known example is the zero-energy flat band existing on the [110] edge of the cuprate  $d$ -wave superconductors [92,93]. These are Andreev bound states at zero-energy and existing for all  $k$  values in the edge 1D Brillouin zone bounded by the projections of the bulk superconducting nodes [94–97]. For the cuprate  $d$ -wave superconductors this means a flat band of zero-energy edge states for the [110] edge but not at the [100] or [010] edges. While these edge states are also protected by a topological argument [96], they are much more fragile than those protected by a finite Chern number and can, e.g., be destroyed by edge inhomogeneity. For the zigzag edge we see similarly to the cuprates that a flat band of zero-energy edge states (red) exist between the two bulk nodal points (green). However, the armchair edge at  $\mu < t$  lacks a zero-energy flat band since there is no distance between the 2 bulk nodal points when they are both projected onto the 1D armchair edge Brillouin zone as the bulk nodal points both occur at  $k_y = 0$ , see Fig. 2. However, the armchair edge for  $\mu > t$  has a finite projection, due to a total of 4 bulk nodal points for a Fermi surface around  $\Gamma$ , and we also now find a zero-energy edge flat band.

#### IV. BILAYER GRAPHENE

Given that the  $p + ip'$ -wave state is the only state which exhibits a phase transition between different Chern number regions for monolayer graphene, we choose in the following to focus primarily on this state for the bilayer and trilayer

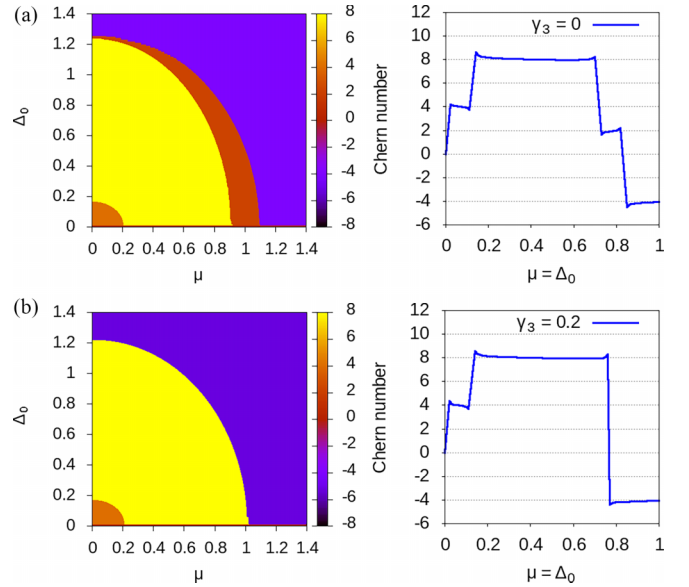


FIG. 7. (Left) Chern number  $\mathcal{C}$  for AB-bilayer graphene with a  $p + ip'$ -wave SC order parameter as a function of  $\mu$  and  $\Delta_0$  and (right) Chern number along the diagonal  $\mu = \Delta_0$  for  $\gamma_1 = 0.2$  and (a) without trigonal warping  $\gamma_3 = 0$  and (b) with trigonal warping  $\gamma_3 = 0.2$ .

graphene systems. However, in Appendix B, we provide some results obtained for bilayer and trilayer graphene with a  $d + id'$ -wave SC order parameter.

First, we consider an AB-stacked bilayer graphene system characterized by a  $p + ip'$ -wave SC order parameter, with an interlayer hopping  $\gamma_1$ , both in the absence and presence of trigonal warping  $\gamma_3$ . We first calculate the Chern number as a function of the chemical potential  $\mu$  and the SC order parameter amplitude  $\Delta_0$ , and we subsequently also study the formation of edge states.

##### A. Bilayer graphene Chern number

In Fig. 7 we plot the Chern number  $\mathcal{C}$  for bilayer graphene with  $p + ip'$ -wave SC order parameter, both with and without trigonal warping,  $\gamma_3$ . For  $\gamma_3 = 0$  we find that phase diagram for the Chern number as a function of  $\mu$  and  $\Delta_0$  contains four different regions as depicted in Fig. 7(a): an orange region with  $\mathcal{C} = 4$ , a yellow region with  $\mathcal{C} = 8$ , a red region with  $\mathcal{C} = 2$ , and, finally, a purple region with  $\mathcal{C} = -4$ . The right plot shows additionally a line-cut at  $\mu = \Delta_0$ . In the presence of warping, i.e., for  $\gamma_3 \neq 0$ , the red region disappears and we end up with only three regions in the phase diagram, see Fig. 7(b). The boundaries between the regions with different values of  $\mathcal{C}$  can be described by the functional form  $\Delta_0 \approx \Delta_c \sqrt{1 - (\mu/\mu_c)^2}$  with critical parameters  $\Delta_c$  and  $\mu_c$  extracted by fitting and given in Table II. These boundaries correspond exactly to the gap closing lines described in Ref. [78], and their dependence on the trigonal warping is described in more detail in this previous work.

We can understand the results in Fig. 7 by again analyzing the normal state band structure, see Appendix A for details, as for the monolayer case. First we ignore  $\gamma_3$  and focus on small  $\Delta_0$ . Then, at the  $K$  and  $K'$  points, the two bands in

TABLE II. Values of the critical parameters  $\Delta_c$  and  $\mu_c$  for mono- and bilayer graphene for  $p + ip'$  pairing.

	$\Delta_c$	$\mu_c$
Monolayer ( $\gamma_1 = \gamma_3 = 0$ )	1.25	1
Normal bilayer ( $\gamma_1 = 0.2$ and $\gamma_3 = 0$ )	0.16	0.2
	1.23	0.9
Warped bilayer ( $\gamma_1 = \gamma_3 = 0.2$ )	1.29	1.1
	0.16	0.2
	1.21	1

bilayer graphene are separated by an energy  $E \sim \gamma_1$ . Thus, for  $\mu < \gamma_1$ , which is the region most likely to be accessed experimentally, there is only one band contributing to the Chern number, yielding  $\mathcal{C} = 4$ , same as for monolayer graphene (two spin species and two Fermi surfaces). At  $\gamma_1 \leq \mu < t - \gamma_1/2$ , both bands are filled and thus contribute to the Chern number, which jumps to 8. In the vicinity of the Lifshitz transition we have now also a splitting of the bands. As a consequence, for  $t - \gamma_1/2 \leq \mu \leq t + \gamma_1/2$  we have one band which contributes with two Fermi surfaces centered around the  $K$  and  $K'$  points and thus a total of  $\mathcal{C} = 4$ , while a second band has its Fermi surface centered around  $\Gamma$  and contributes a  $\mathcal{C} = -2$ . The total Chern is thus expected to be  $\mathcal{C} = 4 - 2 = 2$ , as also seen in Fig. 7(a). Next turning on the trigonal warping  $\gamma_3 \neq 0$ , there is a splitting of the bands at the  $M$  points and hence the trigonal warping strongly influences the size of the  $\mathcal{C} = 2$  region. In fact, if  $\gamma_1 \approx \gamma_3$ , then this region shrinks to zero. Finally, for  $\mu > t + \gamma_1/2$  both bands have a Fermi surface centered around  $\Gamma$ , and we find  $\mathcal{C} = -4$ . For larger  $\Delta_0$  the above transition points follows the gap closing lines established in Table II.

Before moving on with studying the edge spectrum, we make two interesting extensions. First, we would like to understand how these above results are modified if the  $p + ip'$ -wave state stems from a NNN pairing range rather from the used NN pairing. This is important to address since NNN range may be preferred over the NN coupling, especially in multi-layer graphene [28,75]. The details for the Hamiltonian with an NNN SC order parameter are provided in Ref. [78]. The gap closing analysis in Ref. [78] indicates that the main difference between the NNN and NN pairing is a gap closing as a function of  $\mu$ , but notably independent of  $\Delta_0$ . We thus expect also a phase diagram for which the Chern number is independent of  $\Delta_0$ . This is verified in Fig. 8 where we observe the same topological phases for NNN pairing as for NN pairing: an orange region with  $\mathcal{C} = 4$ , a yellow region with  $\mathcal{C} = 8$ , a red region with  $\mathcal{C} = 2$ , and a purple region with  $\mathcal{C} = -4$ , but these are notably only affected by changing  $\mu$ , not by the value of  $\Delta_0$ .

Second, it is possible that a phase  $\phi = \pi$  arises in certain situations between the SC order parameters in different graphene layers. Such phase difference has for example been noted in twisted bilayer graphene [25,98,99]. While no such phase difference has been observed in regular graphene we believe it is still interesting here to understand its role for the topological phase diagram. Thus in Fig. 9 we plot the value of the Chern number for bilayer graphene with NN  $d + id'$ -

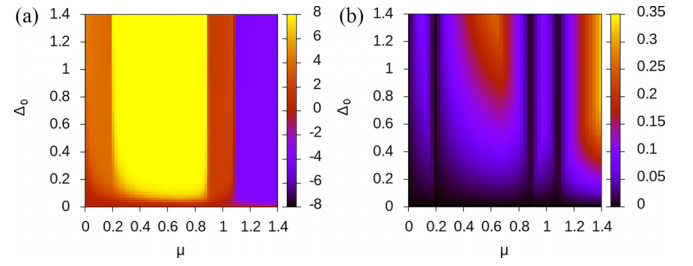


FIG. 8. (a) Chern number and (b) energy gap for AB-bilayer graphene with a  $p + ip'$ -wave SC order parameter on NNN bonds as a function of  $\mu$  and  $\Delta_0$  for  $\gamma_1 = 0.2$ ,  $\gamma_3 = 0$ .

and  $p + ip'$ -wave state when there is phase difference  $\phi = \pi$  between the SC order parameters in the two graphene layers. We see that the main effect of this  $\pi$ -phase difference is the destruction of the topological phase at small values of  $\Delta_0$ , such that a trivial region with  $\mathcal{C} = 0$  is formed for small  $\Delta_0$ . This is particularly interesting to note, since it indicates that such a SC dephasing may destroy the topological properties of a multilayer system in the experimentally accessible regime.

## B. Bilayer graphene edge states

Moving on to the edge spectrum for bilayer graphene, we show in Fig. 10 the edge correction to the spectral function for a  $p + ip'$ -wave SC state without warping,  $\gamma_3 = 0$ , in the four different Chern number regions identified in Fig. 7(a). For the armchair edge, the number of edge states corresponds indeed to the absolute value of the Chern number since one counts four edge states in Fig. 10(a), eight edge states in Fig. 10(b), two edge states in Fig. 10(c), and four edge states in Fig. 10(d) which correspond to regions in the phase diagram inside which  $\mathcal{C}$  is equal to 4, 8, 2, and  $-4$ , respectively (all states are spin-degenerate but all plots also shows the edge spectrum for two edges with counterpropagating edge states, just as for monolayer graphene). However, for a zigzag edge one difference arises in Fig. 10(c), corresponding to values of  $\mu$  and  $\Delta_0$  that are located in the red  $\mathcal{C} = 2$  region of Fig. 7(a). While  $\mathcal{C} = 2$ , we can count six states crossing at zero energy. Such a situation has also been described in Ref. [89], where it was found that in some situations extra crossings may arise that are not topologically protected such that they can be removed by disorder or other modifications. Direct tight-binding calculations of the band structures show that this

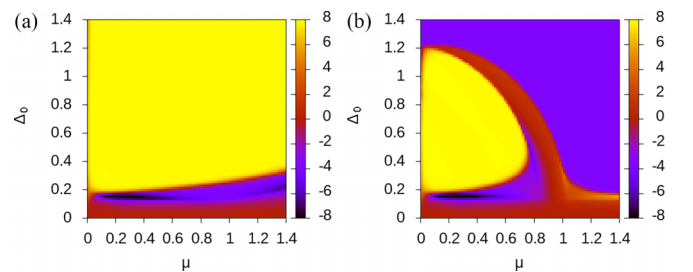


FIG. 9. Chern number  $\mathcal{C}$  for AB-bilayer graphene with (a)  $d + id'$ - and (b)  $p + ip'$ -wave SC order parameter as a function of  $\mu$  and  $\Delta_0$  at  $\gamma_1 = 0.2$  and  $\gamma_3 = 0$ , with a phase difference  $\phi = \pi$  between the SC orders in the two graphene layers.



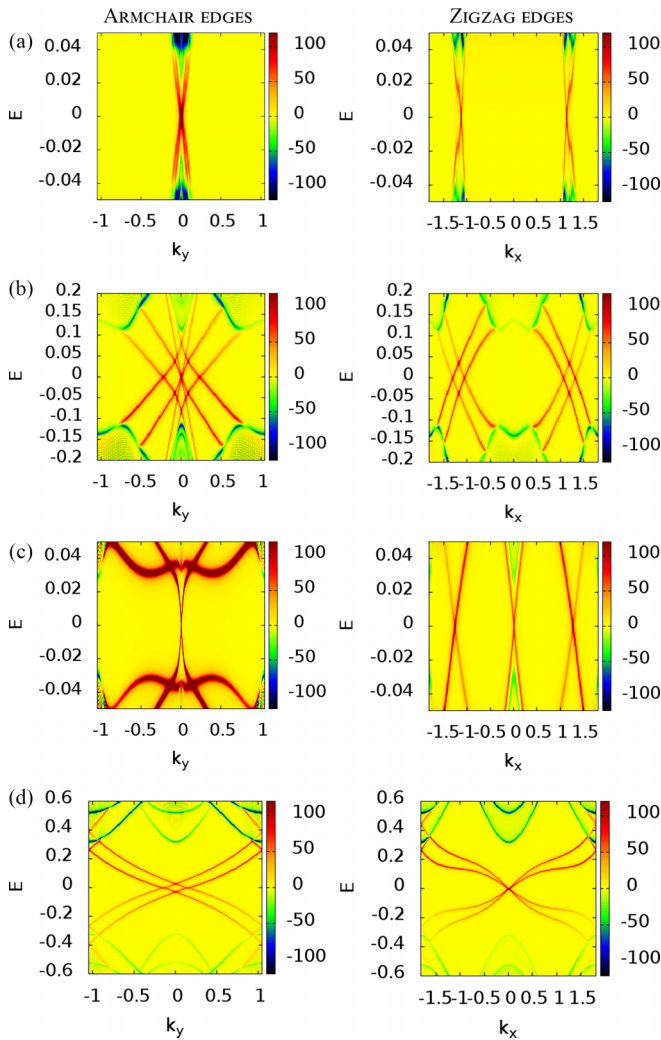


FIG. 10. Edge correction to the spectral function for AB-bilayer graphene with a  $p + ip'$ -wave SC order parameter with  $\gamma_1 = 0.2$  and  $\gamma_3 = 0$  at (a)  $\Delta_0 = \mu = 0.1$  corresponding to  $\mathcal{C} = 4$ , (b)  $\Delta_0 = \mu = 0.6$  corresponding to  $\mathcal{C} = 8$ , (c)  $\Delta_0 = \mu = 0.8$  corresponding to  $\mathcal{C} = 2$ , and (d)  $\Delta_0 = \mu = 1.1$  corresponding to  $\mathcal{C} = -4$ .

is what happens here as well and only the crossing at  $k_x = 0$  is topologically protected; each topologically protected band can in principle cross zero energy an odd number of times.

## V. TRILAYER GRAPHENE

Next we consider trilayer graphene with both ABA and ABC stacking, again with a  $p + ip'$ -wave SC order parameter and with interlayer hopping  $\gamma_1$ . We calculate the Chern number and study the edge states first in the absence and then in the presence of trigonal warping  $\gamma_3$ .

### A. Trilayer graphene Chern number

For ABA-stacked trilayer graphene without trigonal warping ( $\gamma_3 = 0$ ), the phase diagram for the Chern number contains five different regions as depicted in Fig. 11(a): a light-orange region with  $\mathcal{C} = 8$ , a yellow region with  $\mathcal{C} = 12$ , a dark-orange region with  $\mathcal{C} = 6$ , a red region with  $\mathcal{C} = 0$ ,

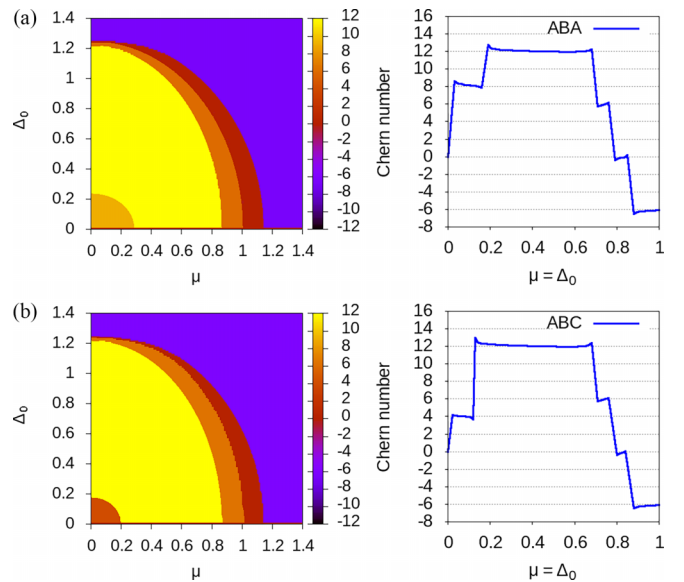


FIG. 11. (Left) Chern number  $\mathcal{C}$  for (a) ABA-stacked and (b) ABC-stacked trilayer graphene with a  $p + ip'$ -wave SC order parameter as a function of  $\mu$  and  $\Delta_0$  and (right) Chern number along the diagonal  $\mu = \Delta_0$  for  $\gamma_1 = 0.2$  and  $\gamma_3 = 0$ .

and, finally, a purple region with  $\mathcal{C} = -6$ . For ABC-stacked trilayer graphene without warping the phase diagram for the Chern number presented in Fig. 11(b) and has a similar appearance except that at low energy we find  $\mathcal{C} = 4$  rather than  $\mathcal{C} = 8$ . To understand the phase diagrams, we also perform similar calculations for tetralayer ( $L = 4$ ) and pentalayer ( $L = 5$ ) graphene systems, with results reported in Appendix C. We note that a Chern number of 4 for  $\mu < \gamma_1$  is only possible for a fully rhombohedral stacking, i.e., ABC for bilayer, ABCA for

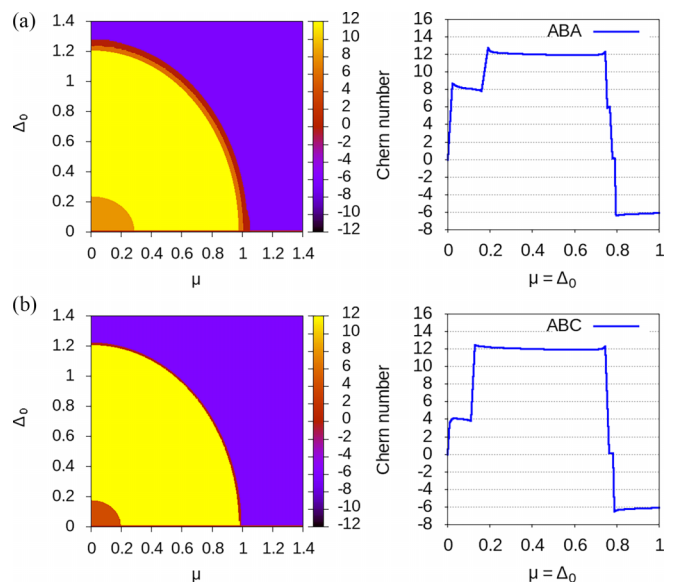


FIG. 12. (Left) Chern number  $\mathcal{C}$  for (a) ABA-stacked and (b) ABC-stacked trilayer graphene with  $p + ip'$  SC order parameter as a function of  $\mu$  and  $\Delta_0$  and (right) Chern number along the diagonal  $\mu = \Delta_0$  for  $\gamma_1 = 0.2$  and  $\gamma_3 = 0.2$ .

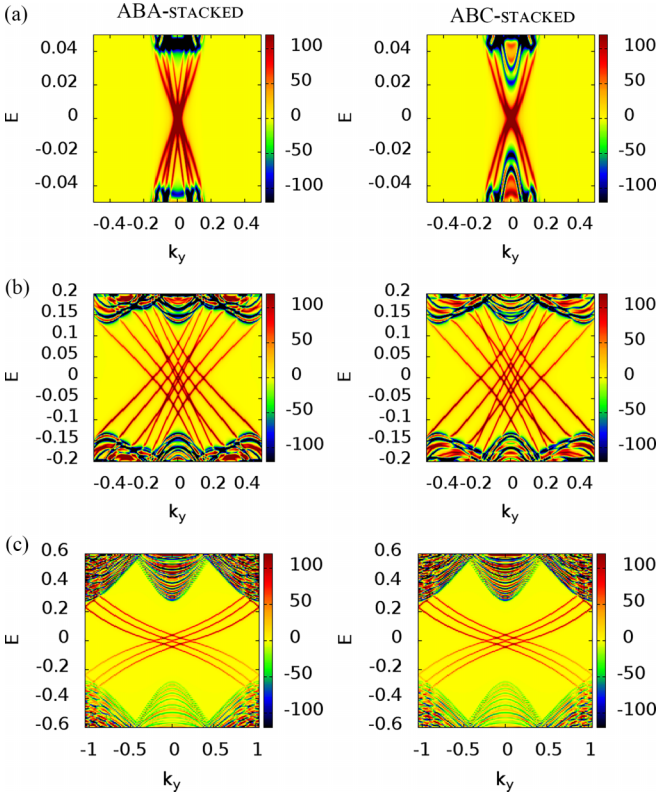


FIG. 13. Edge correction to the spectral function for trilayer graphene with a  $p + ip'$ -wave SC order parameter in trilayer graphene with armchair edges with  $\gamma_1 = 0.2$  and  $\gamma_3 = 0$  at (a)  $\Delta_0 = \mu = 0.1$  corresponding to  $\mathcal{C} = 8$  for ABA-stacked and to  $\mathcal{C} = 4$  for ABC-stacked trilayer, (b)  $\Delta_0 = \mu = 0.4$  corresponding to  $\mathcal{C} = 12$ , and (c)  $\Delta_0 = \mu = 1.1$  corresponding to  $\mathcal{C} = -6$ .

tetralayer and ABCAB for pentalayer graphene. The fact that the Chern number in this region is universally  $\mathcal{C} = 4$  and does not depend on the number of layers is quite a remarkable result, and could serve as a way to identify this type of stacking which has particularly different topological properties.

Next we again note the influence of the normal state band structure. For small values of  $\Delta_0$ ,  $\mathcal{C}$  is simply  $\pm 2$  times

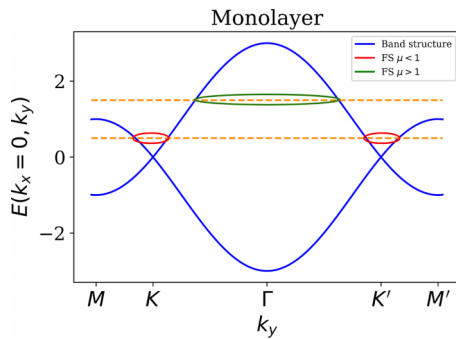


FIG. 14. Band structure for monolayer graphene. The orange dotted lines denote the Fermi level for a regime in which the normal state Fermi surface is described by two circles centered around the  $K$  points (denoted in red,  $\mu < 1$ ), and respectively a single circle centered around the  $\Gamma$  point ( $\mu > 1$ ).

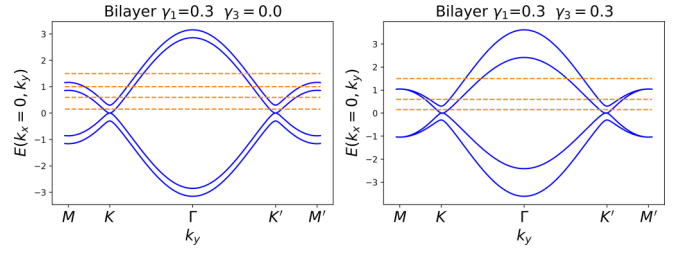


FIG. 15. Band structure for bilayer graphene (left) without trigonal warping, and (right) with trigonal warping. Note that close to the  $M$  point the splitting of the bands is reduced in the presence of  $\gamma_3$ , consistent with the reduction of the size of the regions with a Chern number of 6 and 0.

the number of occupied bands per Fermi surface at a specific value  $\mu$ . For  $\mu < \gamma_1$  we have one occupied band in ABC-stacked graphene and two bands for ABA stacking (see Appendix A). For ABC stacking the band is quasiflat close to the two Dirac points, while for ABA stacking we have a linear band and a quadratic band. Each band exhibits two Fermi surfaces close to the two  $K$  and  $K'$  Dirac points and is also spin degenerate. Hence the value  $\mathcal{C} = 4$  for ABC-stacked graphene, and  $\mathcal{C} = 8$  for ABA-stacked graphene. For the yellow region,  $\gamma_1 \leq \mu \lesssim t$ , we have three filled bands and thus  $\mathcal{C} = 12$  for all types of trilayers. For the stairway regions around  $\mu = t$  there can either be two filled bands with two Fermi surfaces each centered at the  $K$  and  $K'$  points respectively and one band with a single Fermi surface centered around  $\Gamma$ , or vice versa, giving  $\mathcal{C} = 2(2 \times 2 - 1) = 6$  and  $\mathcal{C} = 2(2 - 2) = 0$  respectively. For large  $\mu \gtrsim t$  we always have three bands with their Fermi surfaces centered around  $\Gamma$  yielding  $\mathcal{C} = -6$ . This means that the two dominating regions in the phase diagram have Chern numbers either 4 times (yellow) or  $-2$  times (purple) the number of layers. This result also hold for tetra- and pentalayer graphene, see Appendix C. For trilayer graphene with warping included, here using  $\gamma_3 = 0.2$ , the dark-orange and red regions separating the yellow region with  $\mathcal{C} = 12$  and purple region with  $\mathcal{C} = -6$  are strongly modified as seen in Fig. 12. In the case of ABA-stacked trilayer, the widths of the dark-orange and red regions are both reduced, while for ABC-stacked trilayer the width of the red region is reduced whereas the dark-orange region entirely disappears. For completeness we give the critical parameters  $\Delta_c$  and  $\mu_c$  characterizing the boundaries of equation  $\Delta_0 = \Delta_c \sqrt{1 - (\mu/\mu_c)^2}$  between the regions with different values for  $\mathcal{C}$  in in Table III.

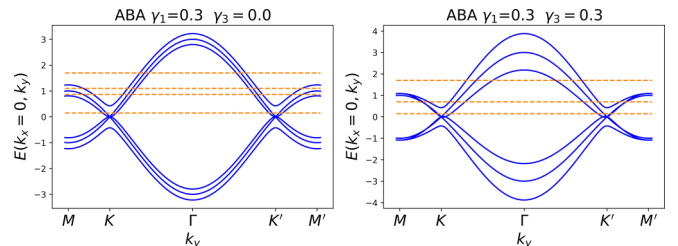


FIG. 16. Band structure for ABA trilayer graphene (left) without trigonal warping, and (right) with trigonal warping.

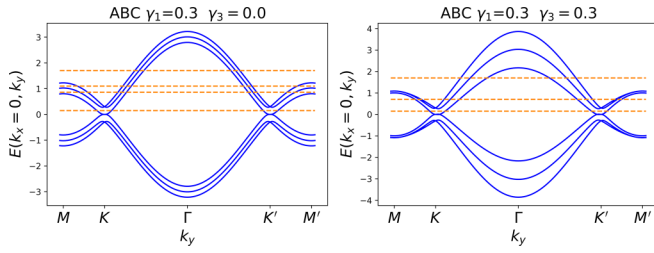


FIG. 17. Band structure for ABC trilayer graphene (left) without trigonal warping, and (right) with trigonal warping

### B. Trilayer graphene edge states

Finally we also report the edge state spectrum for trilayer graphene with a NN  $p + ip'$ -wave SC order parameter. The correction to the spectral function for the trilayer graphene with a line impurity along an armchair edge is plotted in Fig. 13 for both ABA-stacked and ABC-stacked stacking. For  $\mu = \Delta_0 = 0.1$  (a), we obtain eight edge states for ABA stacking, whereas we find four edge state for ABC-stacking, in full agreement with the Chern number  $\mathcal{C}$  extracted from Fig. 11. For  $\mu = \Delta_0 = 0.4$  and  $\mu = \Delta_0 = 1.1$ , both ABA-stacked and ABC-stacked trilayer graphene exhibit 12 and 6 edges states, respectively, again in perfect agreement with the value of  $\mathcal{C}$  calculated in the phase diagram in Fig. 11. Similarly to the cases of monolayer and bilayer graphene, we observe also for trilayer graphene a gap closing each time that the number of edge states or Chern number changes.

## VI. SUMMARY

We calculated the Chern number and the edge state spectral function for monolayer, bilayer and ABA- and ABC-stacked trilayer graphene in the presence of a chiral  $p + ip'$ - or  $d + id'$ -wave SC order parameter. We showed that the absolute value of the Chern number is in full agreement with the number of edge states. We also showed that for the  $p + ip'$ -wave state one or more phase transitions occur in the Chern number when turning the SC order parameter amplitude  $\Delta_0$  or the chemical potential  $\mu$ , with the transitions corresponding to gap closings in the energy spectrum. For multilayer graphene with  $p + ip'$ -wave pairing, the number of regions in the phase diagram increases with the number of layers, with the size of the regions strongly affected by the trigonal warping. Notably, the largest phases have a Chern number either four times or minus twice the number of layers. In addition, we noted

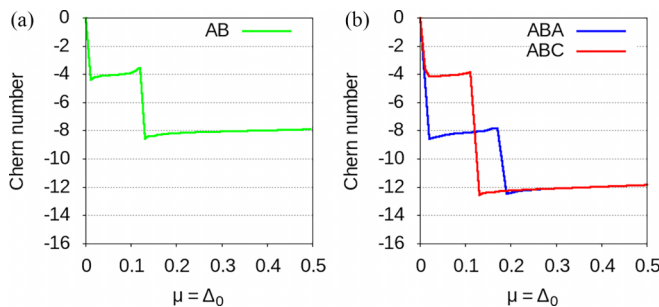


FIG. 18. Chern number  $\mathcal{C}$  for (a) bi- and (b) trilayer graphene with a  $d + id'$ -wave SC order parameter, plotted along the diagonal  $\mu = \Delta_0$  at  $\gamma_1 = 0.2$  and  $\gamma_3 = 0$ .

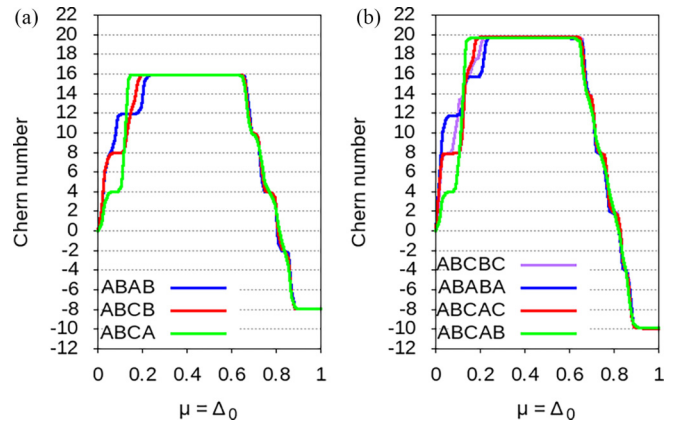


FIG. 19. Chern number  $\mathcal{C}$  for (a) tetra- and (b) pentalayer graphene with a  $p + ip'$ -wave SC order parameter, plotted along the diagonal  $\mu = \Delta_0$  at  $\gamma_1 = 0.2$  and  $\gamma_3 = 0$  with the possible stacking choices [100] in different colors.

the existence of a peculiar low-energy region whose Chern number (4) does not depend on the number of layers for ABC stacking and whose size is proportional to the value of interlayer coupling. Furthermore, we find a strong difference between NN and NNN  $p + ip'$ -wave pairing. This difference stems mainly from the fact that for NNN coupling the phases, as well as the gap closings [78], are not affected by the value of the SC order parameter amplitude, but only by the value of the chemical potential. We also took into account a phase difference of  $\pi$  between layers in bilayer systems and then found that this suppresses the topological character of both the  $p + ip'$ - and the  $d + id'$ -wave SC systems at small values of the order parameter amplitude. Last, we showed that the topological properties of all graphene systems at not too large SC gap values, in particular the Chern number and the number of edge states, can be determined directly from the topology of the normal state Fermi surface. Impurity-induced subgap states and quasiparticle interference patterns have also been calculated in such systems [101].

TABLE III. Values of the critical parameters  $\Delta_c$  and  $\mu_c$  for ABA- and ABC-stacked trilayer graphene for  $p + ip'$  pairing.

	$\Delta_c$	$\mu_c$
	0.23	0.28
Normal ABC trilayer ( $\gamma_1 = 0.2$ and $\gamma_3 = 0$ )	1.21	0.86
	1.24	1
	1.3	1.15
Warped ABA trilayer ( $\gamma_1 = \gamma_3 = 0.2$ )	0.17	0.19
	1.21	0.86
	1.24	1
	1.3	1.15
Warped ABC trilayer ( $\gamma_1 = \gamma_3 = 0.2$ )	0.23	0.28
	1.2	0.97
	1.23	1
	1.27	1.03
	0.17	0.19
Warped ABC trilayer ( $\gamma_1 = \gamma_3 = 0.2$ )	1.2	0.97
	1.23	1

### ACKNOWLEDGMENTS

We thank N. Campion for his contribution to the parallelization of our codes. We acknowledge financial support from the Swedish Research Council (Vetenskapsrådet Grant No. 2018-03488) and the Knut and Alice Wallenberg Foundation through the Wallenberg Academy Fellows program and thank the Centre de Calcul Intensif d'Aix-Marseille for granting access to high performance computing resources. N.S. thanks the National Science Centre (NCN, Poland) for funding under the Grant No. 2018/29/B/ST3/01892. O.A.A. acknowledges funding from NanoLund.

### APPENDIX A: NORMAL STATE BAND STRUCTURE

Figures 14–17 give the normal state band structure for monolayer graphene, as well as for bilayer graphene, and trilayer graphene with ABA and ABC stacking. This will help us to make the correspondence to the Chern number in the  $p + ip'$  SC state, as indicated in the main text. The orange dotted lines denote the Fermi level for the various regimes described in the main text, indicating the number of filled bands and respectively the topology of the normal state Fermi surface, for example if it corresponds to one or two separate regions.

### APPENDIX B: CHERN NUMBER FOR BILAYER AND TRILAYER GRAPHENE WITH A $d + id'$ -WAVE SC ORDER PARAMETER

For bilayer and trilayer graphene with a  $d + id'$ -wave SC order parameter, the Chern number  $\mathcal{C}$  varies with  $\mu$  and  $\Delta_0$ , contrary to what one has found for monolayer graphene, for which  $\mathcal{C}$  is constant and equal to  $-4$ , see Fig. 3(a). Indeed, for bilayer graphene in the low  $(\mu, \Delta_0)$  region,  $\mathcal{C}$  is equal to  $-4$ , and it changes to  $-8$  with increasing  $\mu = \Delta_0$ , see Fig. 18(a). For trilayer graphene in the low  $(\mu, \Delta_0)$  region,  $\mathcal{C}$  is equal to  $-4$  or  $-8$  for an ABC, and respectively an ABA stacking. It subsequently changes to  $-12$  for large  $\mu = \Delta_0$ , see Fig. 18(b).

### APPENDIX C: CHERN NUMBER FOR TETRA- AND PENTALAYER GRAPHENE WITH $p + ip'$ -WAVE SC ORDER PARAMETER

In this Appendix we present the Chern number  $\mathcal{C}$ , extracted at  $\mu = \Delta_0$  for both tetralayer and pentalayer graphene with a  $p + ip'$ -wave SC order parameter. We plot the Chern number

TABLE IV. Chern number  $\mathcal{C}$  for monolayer and different multi-layer graphene systems in the three largest regimes of the  $(\mu, \Delta_0)$  phase diagram: the Chern value in the low  $\mu$  region (i) with  $\mu, \Delta_0 \lesssim \gamma_1$ , the Chern value in the intermediate region (ii) with  $\gamma_1 \lesssim \mu, \Delta_0 \lesssim t$ , and the Chern value in the high  $\mu$  region (iii) with  $\mu, \Delta_0 \gtrsim t$ .

System	Region (i)	Region (ii)	Region (iii)
Monolayer	4	4	$-2$
Bilayer AB	4	8	$-4$
Trilayer ABA	8	12	$-6$
Trilayer ABC	4	12	$-6$
Tetralayer ABAB	12	16	$-8$
Tetralayer ABCB	8	16	$-8$
Tetralayer ABCA	4	16	$-8$
Pentalayer ABCBC	8	20	$-10$
Pentalayer ABABA	12	20	$-10$
Pentalayer ABCAC	8	20	$-10$
Pentalayer ABCAB	4	20	$-10$

in Fig. 19, with the results summarized in Table IV. We conclude that there are only a finite number of possible values for the Chern number in region (i), i.e., the region with  $\mu, \Delta_0 \lesssim \gamma_1$ :  $\mathcal{C} = 4n$  with  $n \in [1, L - 1]$  being the number of occupied bands with two Fermi surfaces centered around the  $K$  and  $K'$  points, and  $L$  the number of layers. Note that a Chern number of 4 is only possible for a fully rhombohedral stacking, i.e., ABCA for tetralayer and ABCAB for pentalayer graphene. For rhombohedral graphene this value does not depend on the number of layers and is unique in region (i). On the other hand, the Chern number in the intermediate  $\mu/\Delta_0$  region (ii), for which  $\gamma_1 \lesssim \mu, \Delta_0 \lesssim t$ , is given by four times the number of layers:  $\mathcal{C} = 4L$  because all the filled bands for all types of stacking have two Fermi surfaces centered around the two  $K$  and  $K'$  points and a Chern number of 4 each. In the large  $\mu/\Delta_0$  region (iii),  $\mu, \Delta_0 \gtrsim t$ , the Chern number seems also to follow a similar pattern being given by two times of number of layers:  $\mathcal{C} = -2L$  because all occupied bands have a Fermi surface centered around the  $\Gamma$  point and a Chern number of  $-2$ . The stairway region in-between regions (ii) and (iii) situated in the vicinity of  $\mu, \Delta \approx t$ , show a quantized value of  $\mathcal{C}$  equal to  $4(L - \ell) - 2\ell = 4L - 6\ell$  with  $\ell \in [1, L - 1]$  being the number of filled bands with one Fermi surface centered around the  $\Gamma$  point for which  $\mathcal{C} = -2$ , and  $L - \ell$  being the number of filled bands with two Fermi surfaces centered around the  $K$  and  $K'$  points for which  $\mathcal{C} = 4$ .

- [1] Y. Cao, V. Fatemi, S. Fang, K. Watanabe, T. Taniguchi, E. Kaxiras, and P. Jarillo-Herrero, Unconventional superconductivity in magic-angle graphene superlattices, *Nature (Lond.)* **556**, 43 (2018).
- [2] H. Zhou, T. Xie, T. Taniguchi, K. Watanabe, and A. F. Young, Superconductivity in rhombohedral trilayer graphene, *Nature (Lond.)* **598**, 434 (2021).
- [3] M. Oh, K. P. Nuckolls, D. Wong, R. L. Lee, X. Liu, K. Watanabe, T. Taniguchi, and A. Yazdani, Evidence for unconventional superconductivity in twisted bilayer graphene, *Nature (Lond.)* **600**, 240 (2021).
- [4] H. C. Po, L. Zou, A. Vishwanath, and T. Senthil, Origin of Mott insulating behavior and superconductivity in twisted bilayer graphene, *Phys. Rev. X* **8**, 031089 (2018).
- [5] F. Guinea and N. R. Walet, Electrostatic effects, band distortions, and superconductivity in twisted graphene bilayers, *Proc. Natl. Acad. Sci. USA* **115**, 13174 (2018).
- [6] F. Wu, A. H. MacDonald, and I. Martin, Theory of phonon-mediated superconductivity in twisted bilayer graphene, *Phys. Rev. Lett.* **121**, 257001 (2018).
- [7] T. J. Peltonen, R. Ojajarvi, and T. T. Heikkilä, *Phys. Rev. B* **98**, 220504(R) (2018).

- [8] D. M. Kennes, J. Lischner, and C. Karrasch, Strong correlations and  $d + id$  superconductivity in twisted bilayer graphene, *Phys. Rev. B* **98**, 241407(R) (2018).
- [9] X. Lu, P. Stepanov, W. Yang, M. Xie, M. A. Aamir, I. Das, C. Urgell, K. Watanabe, T. Taniguchi, G. Zhang, A. Bachtold, A. H. MacDonald, and D. K. Efetov, Superconductors, orbital magnets and correlated states in magic-angle bilayer graphene, *Nature (Lond.)* **574**, 653 (2019).
- [10] M. Yankowitz, S. Chen, H. Polshyn, Y. Zhang, K. Watanabe, T. Taniguchi, D. Graf, A. F. Young, and C. R. Dean, Tuning superconductivity in twisted bilayer graphene, *Science* **363**, 1059 (2019).
- [11] G. Chen, A. L. Sharpe, P. Gallagher, I. T. Rosen, E. J. Fox, L. Jiang, B. Lyu, H. Li, K. Watanabe, T. Taniguchi, J. Jung, Z. Shi, D. Goldhaber-Gordon, Y. Zhang, and F. Wang, Signatures of tunable superconductivity in a trilayer graphene moiré superlattice, *Nature (Lond.)* **572**, 215 (2019).
- [12] M. Alidoust, M. Willatzen, and A.-P. Jauho, Symmetry of superconducting correlations in displaced bilayers of graphene, *Phys. Rev. B* **99**, 155413 (2019).
- [13] L. Balents, C. R. Dean, D. K. Efetov, and A. F. Young, Superconductivity and strong correlations in moiré flat bands, *Nat. Phys.* **16**, 725 (2020).
- [14] E. Y. Andrei and A. H. MacDonald, Graphene bilayers with a twist, *Nat. Mater.* **19**, 1265 (2020).
- [15] M. Christos, S. Sachdev, and M. S. Scheurer, Superconductivity, correlated insulators, and Wess–Zumino–Witten terms in twisted bilayer graphene, *Proc. Natl. Acad. Sci. USA* **117**, 29543 (2020).
- [16] D. V. Chichinadze, L. Classen, and A. V. Chubukov, Nematic superconductivity in twisted bilayer graphene, *Phys. Rev. B* **101**, 224513 (2020).
- [17] Y. Cao, D. Rodan-Legrain, J. M. Park, N. F. Q. Yuan, K. Watanabe, T. Taniguchi, R. M. Fernandes, L. Fu, and P. Jarillo-Herrero, Nematicity and competing orders in superconducting magic-angle graphene, *Science* **372**, 264 (2021).
- [18] X. Wu, W. Hanke, M. Fink, M. Klett, and R. Thomale, Harmonic fingerprint of unconventional superconductivity in twisted bilayer graphene, *Phys. Rev. B* **101**, 134517 (2020).
- [19] T. Yu, D. M. Kennes, A. Rubio, and M. A. Sentef, Nematicity arising from a chiral superconducting ground state in magic-angle twisted bilayer graphene under in-plane magnetic fields, *Phys. Rev. Lett.* **127**, 127001 (2021).
- [20] E. Khalaf, S. Chatterjee, N. Bultinck, M. P. Zaletel, and A. Vishwanath, Charged skyrmions and topological origin of superconductivity in magic-angle graphene, *Sci. Adv.* **7**, eabf5299 (2021).
- [21] T. Cea and F. Guinea, Coulomb interaction, phonons, and superconductivity in twisted bilayer graphene, *Proc. Natl. Acad. Sci. USA* **118**, e2107874118 (2021).
- [22] Y.-Z. Chou, F. Wu, J. D. Sau, and S. Das Sarma, Correlation-induced triplet pairing superconductivity in graphene-based moiré systems, *Phys. Rev. Lett.* **127**, 217001 (2021).
- [23] A. Fischer, Z. A. H. Goodwin, A. A. Mostofi, J. Lischner, D. M. Kennes, and L. Klebl, Unconventional superconductivity in magic-angle twisted trilayer graphene, *npj Quant. Mater.* **7**, 5 (2022).
- [24] H. Kim, Y. Choi, C. Lewandowski, A. Thomson, Y. Zhang, R. Polski, K. Watanabe, T. Taniguchi, J. Alicea, and S. Nadj-Perge, Evidence for unconventional superconductivity in twisted trilayer graphene, *Nature (Lond.)* **606**, 494 (2022).
- [25] T. Löthman, J. Schmidt, F. Parhizgar, and A. M. Black-Schaffer, Nematic superconductivity in magic-angle twisted bilayer graphene from atomistic modeling, *Commun. Phys.* **5**, 92 (2022).
- [26] T. Cea, P. A. Pantaleón, V. o. T. Phong, and F. Guinea, Superconductivity from repulsive interactions in rhombohedral trilayer graphene: A Kohn-Luttinger-like mechanism, *Phys. Rev. B* **105**, 075432 (2022).
- [27] S. Chatterjee, T. Wang, E. Berg, and M. P. Zaletel, Inter-valley coherent order and isospin fluctuation mediated superconductivity in rhombohedral trilayer graphene, *Nat. Commun.* **13**, 6013 (2022).
- [28] Y.-Z. Chou, F. Wu, J. D. Sau, and S. Das Sarma, Acoustic-phonon-mediated superconductivity in rhombohedral trilayer graphene, *Phys. Rev. Lett.* **127**, 187001 (2021).
- [29] A. L. Szabó and B. Roy, Metals, fractional metals, and superconductivity in rhombohedral trilayer graphene, *Phys. Rev. B* **105**, L081407 (2022).
- [30] Y.-Z. You and A. Vishwanath, Kohn-Luttinger superconductivity and intervalley coherence in rhombohedral trilayer graphene, *Phys. Rev. B* **105**, 134524 (2022).
- [31] A. Ghazaryan, T. Holder, M. Serbyn, and E. Berg, Unconventional superconductivity in systems with annular Fermi surfaces: Application to rhombohedral trilayer graphene, *Phys. Rev. Lett.* **127**, 247001 (2021).
- [32] D.-C. Lu, T. Wang, S. Chatterjee, and Y.-Z. You, Correlated metals and unconventional superconductivity in rhombohedral trilayer graphene: A renormalization group analysis, *Phys. Rev. B* **106**, 155115 (2022).
- [33] A. Ghazaryan, T. Holder, E. Berg, and M. Serbyn, Multi-layer graphenes as a platform for interaction-driven physics and topological superconductivity, *Phys. Rev. B* **107**, 104502 (2023).
- [34] T. Cea, Superconductivity induced by the intervalley coulomb scattering in a few layers of graphene, *Phys. Rev. B* **107**, L041111 (2023).
- [35] A. M. Black-Schaffer and S. Doniach, Resonating valence bonds and mean-field  $d$ -wave superconductivity in graphite, *Phys. Rev. B* **75**, 134512 (2007).
- [36] C. Honerkamp, Density waves and Cooper pairing on the honeycomb lattice, *Phys. Rev. Lett.* **100**, 146404 (2008).
- [37] R. Nandkishore, L. Levitov, and A. V. Chubukov, Chiral superconductivity from repulsive interactions in doped graphene, *Nat. Phys.* **8**, 158 (2012).
- [38] M. L. Kiesel, C. Platt, W. Hanke, D. A. Abanin, and R. Thomale, Competing many-body instabilities and unconventional superconductivity in graphene, *Phys. Rev. B* **86**, 020507(R) (2012).
- [39] W.-S. Wang, Y.-Y. Xiang, Q.-H. Wang, F. Wang, F. Yang, and D.-H. Lee, Functional renormalization group and variational monte carlo studies of the electronic instabilities in graphene near  $\frac{1}{4}$  doping, *Phys. Rev. B* **85**, 035414 (2012).
- [40] A. M. Black-Schaffer and C. Honerkamp, Chiral  $d$ -wave superconductivity in doped graphene, *J. Phys.: Condens. Matter* **26**, 423201 (2014).

- [41] A. M. Black-Schaffer, W. Wu, and K. Le Hur, Chiral  $d$ -wave superconductivity on the honeycomb lattice close to the mott state, *Phys. Rev. B* **90**, 054521 (2014).
- [42] T. Löthman and A. M. Black-Schaffer, Defects in the  $d + id$ -wave superconducting state in heavily doped graphene, *Phys. Rev. B* **90**, 224504 (2014).
- [43] T. Ma, F. Yang, H. Yao, and H.-Q. Lin, Possible triplet  $p + ip$  superconductivity in graphene at low filling, *Phys. Rev. B* **90**, 245114 (2014).
- [44] A. M. Alsharari and S. E. Ulloa, Inducing chiral superconductivity on honeycomb lattice systems, *J. Phys.: Condens. Matter* **34**, 205403 (2022).
- [45] J. B. Curtis, N. R. Poniatowski, Y. Xie, A. Yacoby, E. Demler, and P. Narang, Stabilizing fluctuating spin-triplet superconductivity in graphene via induced spin-orbit coupling, *Phys. Rev. Lett.* **130**, 196001 (2023).
- [46] S. Wolf, T. Gardener, K. Le Hur, and S. Rachel, Topological superconductivity on the honeycomb lattice: Effect of normal state topology, *Phys. Rev. B* **105**, L100505 (2022).
- [47] M. V. Hosseini and M. Zareyan, Model of an exotic chiral superconducting phase in a graphene bilayer, *Phys. Rev. Lett.* **108**, 147001 (2012).
- [48] M. V. Hosseini, Inhomogeneous superconductivity in the presence of time-reversal symmetry, *Europhys. Lett.* **110**, 47010 (2015).
- [49] A. D. Bernardo, O. Millo, M. Barbone, H. Alpern, Y. Kalcheim, U. Sassi, A. K. Ott, D. D. Fazio, D. Yoon, M. Amado, A. C. Ferrari, J. Linder, and J. W. A. Robinson,  $p$ -wave triggered superconductivity in single-layer graphene on an electron-doped oxide superconductor, *Nat. Commun.* **8**, 14024 (2017).
- [50] O. A. Awoga and A. M. Black-Schaffer, Probing unconventional superconductivity in proximitized graphene by impurity scattering, *Phys. Rev. B* **97**, 214515 (2018).
- [51] D. Perconte, K. Seurre, V. Humbert, C. Ulysse, A. Sander, J. Trastoy, V. Zlatko, F. Godel, P. R. Kidambi, S. Hofmann, X. P. Zhang, D. Bercioux, F. S. Bergeret, B. Dlubak, P. Seneor, and J. E. Villegas, Long-range propagation and interference of  $d$ -wave superconducting pairs in graphene, *Phys. Rev. Lett.* **125**, 087002 (2020).
- [52] D. Perconte, D. Bercioux, B. Dlubak, P. Seneor, F. S. Bergeret, and J. E. Villegas, Superconducting proximity effect in  $d$ -wave cuprate/graphene heterostructures, *Ann. Phys.* **534**, 2100559 (2022).
- [53] M. V. Hosseini and M. Zareyan, Unconventional superconducting states of interlayer pairing in bilayer and trilayer graphene, *Phys. Rev. B* **86**, 214503 (2012).
- [54] C. Xu and L. Balents, Topological superconductivity in twisted multilayer graphene, *Phys. Rev. Lett.* **121**, 087001 (2018).
- [55] A. P. Durajski, K. M. Skoczylas, and R. a. Szczniak, Superconductivity in bilayer graphene intercalated with alkali and alkaline earth metals, *Phys. Chem. Chem. Phys.* **21**, 5925 (2019).
- [56] J. M. Park, Y. Cao, L.-Q. Xia, S. Sun, K. Watanabe, T. Taniguchi, and P. Jarillo-Herrero, Robust superconductivity in magic-angle multilayer graphene family, *Nat. Mater.* **21**, 877 (2022).
- [57] Y.-Z. Chou, F. Wu, J. D. Sau, and S. Das Sarma, Acoustic-phonon-mediated superconductivity in Bernal bilayer graphene, *Phys. Rev. B* **105**, L100503 (2022).
- [58] Y.-Z. Chou, F. Wu, J. D. Sau, and S. Das Sarma, Acoustic-phonon-mediated superconductivity in moiréless graphene multilayers, *Phys. Rev. B* **106**, 024507 (2022).
- [59] H. Zhou, L. Holleis, Y. Saito, L. Cohen, W. Huynh, C. L. Patterson, F. Yang, T. Taniguchi, K. Watanabe, and A. F. Young, Isospin magnetism and spin-polarized superconductivity in Bernal bilayer graphene, *Science* **375**, 774 (2022).
- [60] R. Su, M. Kouri, K. Watanabe, T. Taniguchi, and J. Folk, Superconductivity in twisted double bilayer graphene stabilized by  $WSe_2$ , *Nat. Mater.* (2023), doi: 10.1038/s41563-023-01653-7.
- [61] Y. Zhang, R. Polski, A. Thomson, É. Lantagne-Hurtubise, C. Lewandowski, H. Zhou, K. Watanabe, T. Taniguchi, J. Alicea, and S. Nadj-Perge, Enhanced superconductivity in spin-orbit proximitized bilayer graphene, *Nature (Lond.)* **613**, 268 (2023).
- [62] B. Roy and I. F. Herbut, Unconventional superconductivity on honeycomb lattice: Theory of Kekule order parameter, *Phys. Rev. B* **82**, 035429 (2010).
- [63] S. Wolf, T. L. Schmidt, and S. Rachel, Unconventional superconductivity in the extended Hubbard model: Weak-coupling renormalization group, *Phys. Rev. B* **98**, 174515 (2018).
- [64] T. Huang, L. Zhang, and T. Ma, Antiferromagnetically ordered mott insulator and  $d+id$  superconductivity in twisted bilayer graphene: A quantum Monte Carlo study, *Sci. Bull.* **64**, 310 (2019).
- [65] H. Dai, R. Ma, X. Zhang, T. Guo, and T. Ma, Quantum Monte Carlo study of superconductivity in rhombohedral trilayer graphene under an electric field, *Phys. Rev. B* **107**, 245106 (2023).
- [66] T. Ma, Z. Huang, F. Hu, and H.-Q. Lin, Pairing in graphene: A quantum Monte Carlo study, *Phys. Rev. B* **84**, 121410(R) (2011).
- [67] M. V. Hosseini and M. Zareyan, Graphene-based ferromagnetic superconductors, *Appl. Phys. Lett.* **101**, 252602 (2012).
- [68] J. Linder, A. M. Black-Schaffer, T. Yokoyama, S. Doniach, and A. Sudbø, Josephson current in graphene: Role of unconventional pairing symmetries, *Phys. Rev. B* **80**, 094522 (2009).
- [69] F. M. Pellegrino, G. G. Angilella, and R. Pucci, Pairing symmetry of superconducting graphene, *Eur. Phys. J. B* **76**, 469 (2010).
- [70] M. Alidoust, A.-P. Jauho, and J. Akola, Josephson effect in graphene bilayers with adjustable relative displacement, *Phys. Rev. Res.* **2**, 032074(R) (2020).
- [71] E. Thingstad, A. Kamra, J. W. Wells, and A. Sudbø, Phonon-mediated superconductivity in doped monolayer materials, *Phys. Rev. B* **101**, 214513 (2020).
- [72] J. Vučićević, M. O. Goerbig, and M. V. Milovanović,  $d$ -wave superconductivity on the honeycomb bilayer, *Phys. Rev. B* **86**, 214505 (2012).
- [73] H. Dai, J. Hou, X. Zhang, Y. Liang, and T. Ma, Mott insulating state and  $d + id$  superconductivity in an abc graphene trilayer, *Phys. Rev. B* **104**, 035104 (2021).
- [74] B. Lian, Z. Wang, and B. A. Bernevig, Twisted bilayer graphene: A phonon-driven superconductor, *Phys. Rev. Lett.* **122**, 257002 (2019).

- [75] O. A. Awoga, T. Löthman, and A. Black-Schaffer, Superconductivity and magnetism in the surface states of ABC-stacked multilayer graphene, *Phys. Rev. B* **108**, 144504 (2023).
- [76] A. M. Black-Schaffer, Edge properties and Majorana fermions in the proposed chiral  $d$ -wave superconducting state of doped graphene, *Phys. Rev. Lett.* **109**, 197001 (2012).
- [77] V. Kaladzhyan and C. Bena, Formation of Majorana fermions in finite-size graphene strips, *SciPost Phys.* **3**, 002 (2017).
- [78] E. Pangburn, L. Haurie, A. Crépieux, O. A. Awoga, A. M. Black-Schaffer, C. Pépin, and C. Bena, this issue, Superconductivity in monolayer and few-layer graphene. I. Review of possible pairing symmetries and basic electronic properties, *Phys. Rev. B* **108**, 134514 (2023).
- [79] G. E. Volovik, *Exotic Properties of Superfluid  $^3\text{He}$*  (World Scientific, Singapore, 1992).
- [80] N. Read and D. Green, Paired states of fermions in two dimensions with breaking of parity and time-reversal symmetries and the fractional quantum hall effect, *Phys. Rev. B* **61**, 10267 (2000).
- [81] O. A. Awoga, A. Bouhon, and A. M. Black-Schaffer, Domain walls in a chiral  $d$ -wave superconductor on the honeycomb lattice, *Phys. Rev. B* **96**, 014521 (2017).
- [82] V. Kaladzhyan and C. Bena, Obtaining majorana and other boundary modes from the metamorphosis of impurity-induced states: Exact solutions via the t-matrix, *Phys. Rev. B* **100**, 081106(R) (2019).
- [83] M. Z. Hasan and C. L. Kane, Colloquium: Topological insulators, *Rev. Mod. Phys.* **82**, 3045 (2010).
- [84] X.-L. Qi and S.-C. Zhang, Topological insulators and superconductors, *Rev. Mod. Phys.* **83**, 1057 (2011).
- [85] L. M. Malard, J. Nilsson, D. C. Elias, J. C. Brant, F. Plentz, E. S. Alves, A. H. Castro Neto, and M. A. Pimenta, Probing the electronic structure of bilayer graphene by raman scattering, *Phys. Rev. B* **76**, 201401(R) (2007).
- [86] E. McCann and M. Koshino, The electronic properties of bilayer graphene, *Rep. Prog. Phys.* **76**, 056503 (2013).
- [87] D. J. Thouless, M. Kohmoto, M. P. Nightingale, and M. den Nijs, Quantized Hall conductance in a two-dimensional periodic potential, *Phys. Rev. Lett.* **49**, 405 (1982).
- [88] P. Ghosh, J. D. Sau, S. Tewari, and S. Das Sarma, Non-abelian topological order in noncentrosymmetric superconductors with broken time-reversal symmetry, *Phys. Rev. B* **82**, 184525 (2010).
- [89] N. Sedlmayr, V. Kaladzhyan, C. Dutreix, and C. Bena, Bulk boundary correspondence and the existence of Majorana bound states on the edges of 2D topological superconductors, *Phys. Rev. B* **96**, 184516 (2017).
- [90] S. Pinon, V. Kaladzhyan, and C. Bena, Surface green's functions and boundary modes using impurities: Weyl semimetals and topological insulators, *Phys. Rev. B* **101**, 115405 (2020).
- [91] S. Pinon, Study of edge phenomena through the use of impurities, thesis, Université Paris-Saclay, 2021.
- [92] S. Kashiwaya and Y. Tanaka, Tunnelling effects on surface bound states in unconventional superconductors, *Rep. Prog. Phys.* **63**, 1641 (2000).
- [93] T. Löfwander, V. S. Shumeiko, and G. Wendin, Andreev bound states in high- $T_c$  superconducting junctions, *Supercond. Sci. Technol.* **14**, R53 (2001).
- [94] S. Ryu and Y. Hatsugai, Topological origin of zero-energy edge states in particle-hole symmetric systems, *Phys. Rev. Lett.* **89**, 077002 (2002).
- [95] M. Sato, Y. Tanaka, K. Yada, and T. Yokoyama, Topology of andreev bound states with flat dispersion, *Phys. Rev. B* **83**, 224511 (2011).
- [96] A. C. Potter and P. A. Lee, Edge ferromagnetism from Majorana flat bands: Application to split tunneling-conductance peaks in high- $T_c$  cuprate superconductors, *Phys. Rev. Lett.* **112**, 117002 (2014).
- [97] D. Chakraborty, T. Löfwander, M. Fogelström, and A. M. Black-Schaffer, Disorder-robust phase crystal in high-temperature superconductors stabilized by strong correlations, *npj Quant. Mater.* **7**, 44 (2022).
- [98] F. Wu, Topological chiral superconductivity with spontaneous vortices and supercurrent in twisted bilayer graphene, *Phys. Rev. B* **99**, 195114 (2019).
- [99] A. Fischer, L. Klebl, C. Honerkamp, and D. M. Kennes, Spin-fluctuation-induced pairing in twisted bilayer graphene, *Phys. Rev. B* **103**, L041103 (2021).
- [100] K. G. Wirth, J. B. Hauck, A. Rothstein, H. Kyoseva, D. Siebenkotten, L. Conrads, L. Klebl, A. Fischer, B. Beschoten, C. Stampfer, D. M. Kennes, L. Waldecker, and T. Taubner, Experimental observation of ABCB stacked tetralayer graphene, *ACS Nano* **16**, 16617 (2022).
- [101] E. Pangburn, L. Haurie, A. Crépieux, O. A. Awoga, N. Sedlmayr, A. M. Black-Schaffer, C. Pépin, and C. Bena, this issue, Superconductivity in monolayer and few-layer graphene. III. Impurity-induced subgap states and quasi-particle interference patterns, *Phys. Rev. B* **108**, 134516 (2023).